RESEARCH ARTICLE

Check for updates

Molecular layer-by-layer re-stacking of MoS2–In2Se3 by electrostatic means: assembly of a new layered photocatalyst†

Bryan K. Y. Ng, ‡[a] Cherie C. Y. Wong,‡[a] Wentian Niu,[a] Hector P. Garcia, [b] Yiyang Li, [a] Ping-Luen Ho,[a] Winson C. H. Kuo,[c] Robert A. Taylor,[d] Keita Taniya, [e] Qi Wei,[f] Mingjie Li,[f] Michail Stamatakis *[b] and Shik Chi Edman Tsang *[a]

2D-layered transition metal chalcogenides are useful semiconductors for a wide range of opto-electronic applications. Their similarity as layered structures offers exciting possibility to modify their electronic properties by creating new heterojunction assemblies from layer-by-layer restacking of individual monolayer sheets, however, the lack of specific interaction between these layers could induce phase segregation. Here, we employed a chemical method using n-BuLi to exfoliate MoS_2 and In_2Se_3 into their monolayer-containing colloids in solution. The bulky Se atoms can be selectively leached from In_2Se_3 during Li treatment which gives positively charged surface monolayers in neutral pH whereas the strong polarization of Mo–S with moderate S leaching gives a negatively charged surface. Specific inter-layer electrostatic attraction during their selective assembly gives a controllable atomic AB-type of layer stacking as supported by EXAFS, STEM with super-EDX mapping, TAS/TRPL and DFT calculations. Using this simple but inexpensive bottom-up solution method, a new photocatalyst assembled from layers for photo water splitting can be tailor-made with high activity.

Introduction

2D layered metal chalcogenides have recently attracted great research interest, due to their chemical versatility and their highly tunable electronic and optical properties.[1–7] The layered structure of these materials can grant unique properties outperforming their bulk forms, for example, a direct band gap can be brought by the monolayer rather than the indirect band gap of multilayers.[8] Group IIIA chalcogenides have recently demonstrated outstanding visible light responsivity and electronic structure tunability in theoretical studies.[9] Amongst them, indium selenide (In_2Se_3) has been recognized as an intriguing material. Its reported intrinsic ferroelectricity is said to generate an internal driving force for the spatial separation of photoexcited electrons.[10] On the other hand, the monolayer Group VIB chalcogenides can be metallic or semiconducting depending on their phase. This compelling behavior is due to an interplay between the d-electron count and ligand field splitting in different coordination environments.

The monolayer 2D metal chalcogenides can be synthesised on solid substrates by bottom-up techniques, *via* (metalorganic) chemical vapour deposition (MOCVD/CVD),[11–13] or electro-chemical methods. For their bulk structures, within each layer of metal chalcogenide, the metals and the chalcogenides are covalently bonded, while the van der Waals interaction holds the different layers together.[14] As a result, top-down synthetic protocols to break the weak interlayer interaction for the preparation of monolayer structures such as mechanical methods and exfoliation methods are also commonly reported.[15,16] A simple liquid exfoliation method by using solvent or mixed solvent molecules has been reported, which can apply to a wide range of layered structures.[17] However, the method is unable to prepare single monolayers but only multilayers. Previous works using chemical exfoliation methods by intercalation chemistry can

[a] Wolfson Catalysis Centre, Department of Chemistry, University of Oxford, OX1 3QR, UK. E-mail: edman.tsang@chem.ox.ac.uk

[b] Thomas Young Centre and Department of Chemical Engineering, University College London, Roberts Building, Torrington Place, London, WC1E 7JE, UK. E-mail: m.stamatakis@ucl.ac.uk

[c] Materials Characterization Facility, Texas A&M University, College Station, TX, 77843, USA

[d] Department of Physics, Clarendon Laboratory, Parks Road, Oxford, OX1 3PU, UK

[e] Department of Chemical Science and Engineering, Graduate School of Engineering, Kobe University, 1-1 Rokkodai, Nada, Kobe, 657-8501, Hyogo, Japan

[f] Department of Applied Physics, The Hong Kong Polytechnic University, Hung Hom, Kowloon, Hong Kong, P. R. China

† Electronic supplementary information (ESI) available. See DOI: https://doi.org/10.1039/d2qm01095j

‡ These authors contributed equally.

prepare high quality monolayer materials in solution.[18–20] Besides the increased surface area, the monolayer thickness of the materials also leads to new compelling electronic and optical properties.[21] These exfoliated monolayer materials have been recognised as potential candidates for various applications.[17,22,23]

Chemical exfoliation methods using *n*-butyl lithium treatment with the metal chalcogenides have been widely applied to exfoliate MoS_2 monolayers.[2,24] As Li^0 from *n*-butyl lithium (*n*-BuLi) intercalates into the inter-layers, their distance will swell, and they can subsequently be physically separated into monolayers by sonication. However, they are subjected to rapid restacking at high concentration or upon drying.[25,26] Further modulation of the properties of these monolayers by other materials to form heterojunctions is known to be an excellent strategy to tailor chemical properties and stability.[27] For example, the difference of the chemical potential between the two semiconductors causes band bending at the interface of the junction, which promotes the effective separation of electron–hole pairs in photoexcitation.[28,29] Heterojunction formation can be accomplished by assembling the two materials together, as in the case of MoS_2/p-Si,[30] MoS_2/SnS_2[31] and MoS_2/WSe_2.[32] An exciting method to intercalate with metal atoms to form new covalent interactions has recently been reported.[33]

Currently, these stacked single layered MoS_2 heterojunction materials are mainly synthesised *via* cost and energy intensive chemical/physical vapour deposition (CVD/PVD) methods.[34,35] However, it is more desirable to create multiple heterojunctions from both single layers of A and B of different chalcogenides in solution to form an extensive alternative AB type of restacking with high degree of materials' interfaces. Nevertheless, the lack of specific interaction(s) between two layered materials and the cost/duration of layer-by-layer deposition without phase segregation would be practically difficult to achieve.

In this work, we have demonstrated the self-assembly of exfoliated In_2Se_3 and MoS_2 species by electrostatic interaction. Due to the larger size of the selenide compared to the sulphide, the intralayer covalent interaction would be much weaker for In_2Se_3 compared to MoS_2. This difference in bond strength leads to a higher amount of anion being reduced and leached during exfoliation by *n*-BuLi, resulting in a positively charged surface of anion defective monolayer In_2Se_3. On a different note, MoS_2 is more chemically stable against oxidative leaching possesses a negatively charged monolayer, due to the covalency between polarizing hard Mo^{4+} cations and polarizable soft S^{2-} anions. Thus, multi heterojunctions can be self-assembled in solution based upon the different chemical affinity of the two metal chalcogenides towards lithium intercalation. The formation of this self-assembled multi-heterojunction material is demonstrated by various structural characterization techniques, such as Extended X-ray absorption fine structure (EXAFS), Density functional theory (DFT) calculations and Super energy-dispersive X-ray spectroscopy (Super-EDX). Subsequently, the optical properties of the heterojunction are investigated *via* time-resolved photoluminescence (TRPL) and transient absorption spectroscopy (TAS). It is proved that the formed multi-heterojunction materials from restacking of individual monolayers displays improved activity towards photocatalytic water splitting compared to their parent layers.

Results and discussion

Exfoliating MoS_2 and In_2Se_3

The preparation of exfoliated MoS_2 (ex-MoS_2) In_2Se_3 (ex-In_2Se_3) and restacked MoS_2–In_2Se_3 multi-heterojunction materials is summarized in the methods section along with their experimental testing procedure for water splitting. Bulk MoS_2 and α-In_2Se_3 were chemically exfoliated by lithium intercalation in our previous work.[20,36,37] Typically, characteristic diffraction peaks of collected supernatant colloids are gradually broadened when probed by X-ray diffraction and eventually disappear to a baseline when single layer fakes are formed in the topmost supernatant upon exfoliation and sonication. The TEM images show the sheet-like morphology of the exfoliated samples (Fig. S1, ESI†). Corresponding typical atomic force microscopy (AFM) height profiles and images of the Li treated bulk samples in ESI† Fig. S2 show the formation of single layers of expected monolayer thickness for prolonged treatment.[38] ESI† Fig. S3 shows the absence of a diffraction peak upon Li treatment. The XRD intermittent diffractogram also confirms the low-intensity peaks between $20°$ to $30°$ in ex-In_2Se_3 attributable to In_xSe_y species formed due to leached Se.[39]

Atomic-resolution high-angle annular dark-field scanning transmission electron microscopy (HAADF-STEM) of a selected thin flake of topmost supernatant of ex-MoS_2, viewed along [001] is provided in Fig. 1a, based on Z contrast intensity differences between each column. The corresponding HAADF-STEM simulated image (Fig. 1b) according to the Dr Probe image simulation software package[40] and atomistic modelling (Fig. 1c) confirm its single monolayer pattern. Similarly, the HAADF-STEM image, simulated image and atomistic model for monolayer In_2Se_3 are also presented (Fig. 1d–f). The TEM image and fast Fourier transform diffraction pattern of bulk In_2Se_3 are provided in ESI† Fig. S4 along with its simulation for comparison. A HAADF-STEM image of bulk In_2Se_3 and its simulation is also provided in Fig. S5 (ESI†).

An Infrequent but direct visualization of a sulphur vacancy by HAADF-STEM of the prepared monolayer MoS_2 by Li treatment was reported due to oxidative leaching of the sulphur atom to Li^+ and S^{2-} in solution (Fig. S6, ESI†).[20,36,37] However, the EDX analysis of exfoliated MoS_2 indicated a Mo : S ratio of 1 : 1.8 for the sample, which is close to the theoretical 1 : 2.0 in bulk MoS_2.[41] The retainment of a monolayer MoS_2 structure with good stoichiometry reflects the stronger bonding between Mo and S against such leaching with only a small degree of anion defects. It is interesting to see that for ex-In_2Se_3, both K and L emission lines of the EDX results (ESI† Fig. S7 and Table S1) revealed an In : Se ratio of 87 : 13, which is significantly deviated to the expected ratio of 2 : 3 in bulk In_2Se_3. This suggests that a considerable proportion of the Se is leached out during the exfoliation/sonication process. Electron paramagnetic resonance (EPR) data (Fig. S8, ESI†) indeed confirmed that ex-In_2Se_3 gives a strong signal at $g = 2.0004$, similar to the g-value of a trapped electron ($g = 2.0023$) in Se vacant site whereas the bulk In_2Se_3 phase is EPR silent. This signal in ex-In_2Se_3 gives a strong experimental support to the formation of Se vacancies.[42,43] Such
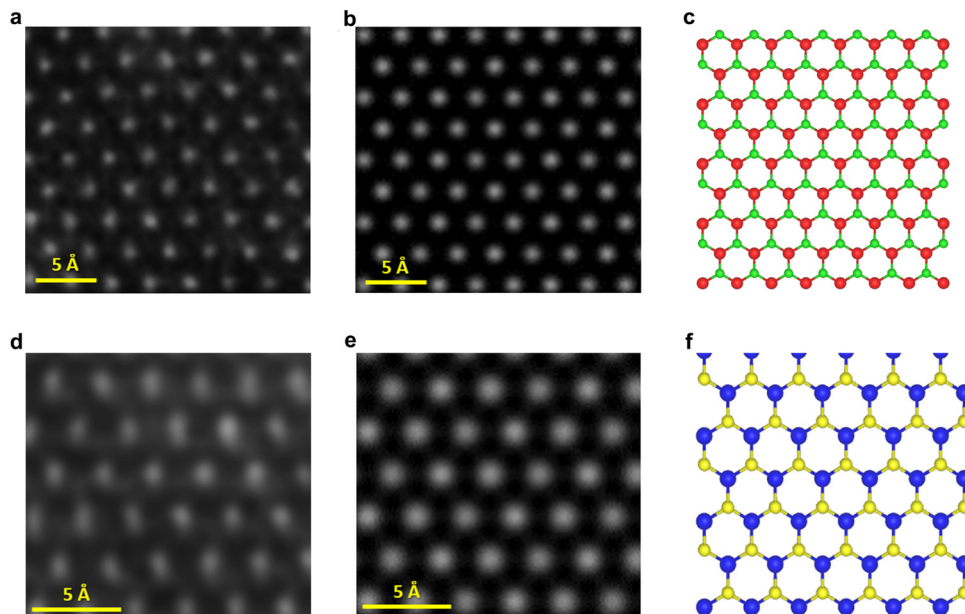
Fig. 1 (a) HAADF-STEM image viewed along [001] plane of monolayer MoS_2. (b) An HAADF image simulation. (c) Atomic model of 2H-MoS_2 for simulation. (d) HAADF-STEM image viewed along [001] plane of monolayer In_2Se_3. (e) An HAADF image simulation and (f) atomic model of 2H-In_2Se_3 for simulation. Colour scheme: Red = Mo, Green = S, Blue = In, Yellow = Se.

an observation is echoed in the X-ray photoelectron spectroscopy (XPS) of bulk and ex-In_2Se_3 (Fig. S9, ESI†). The indium spin–orbit coupling peaks of $3d_{5/2}$ and $3d_{3/2}$ for bulk In_2Se_3 are at 444.9 and 452.5 eV, respectively, corresponding to published values in the literature.[44,45] They are clearly shifted to higher energy of 446.1 and 453.7 eV, indicating an increase in positive charge of the In species, caused by the reduction in the number of selenide counter anions. On the other hand, the Se XPS peak, composed of $3d_{5/2}$ and $3d_{3/2}$, has decreased in binding energy from 58.2 to 55.5 eV for bulk and ex-In_2Se_3, respectively. Because of the reduced Se population, the average charge each selenide ion

receives from indium has increased, resulting in the decreased XPS peak energy.

MoS_2–In_2Se_3 multi-heterojunction

The zeta potentials of ex-MoS_2 and ex-In_2Se_3 solutions were measured (Fig. 2f and ESI† Table S2) to be -35.0 mV and $+21.3$ mV, respectively. It is well-accepted that the more electronegative sulphur atoms found on top and bottom of the exposed monolayer when compared to the trigonal prismatic sandwich molybdenum atoms is expected to induce a negative surface charge for this molecular structure. On the other hand,
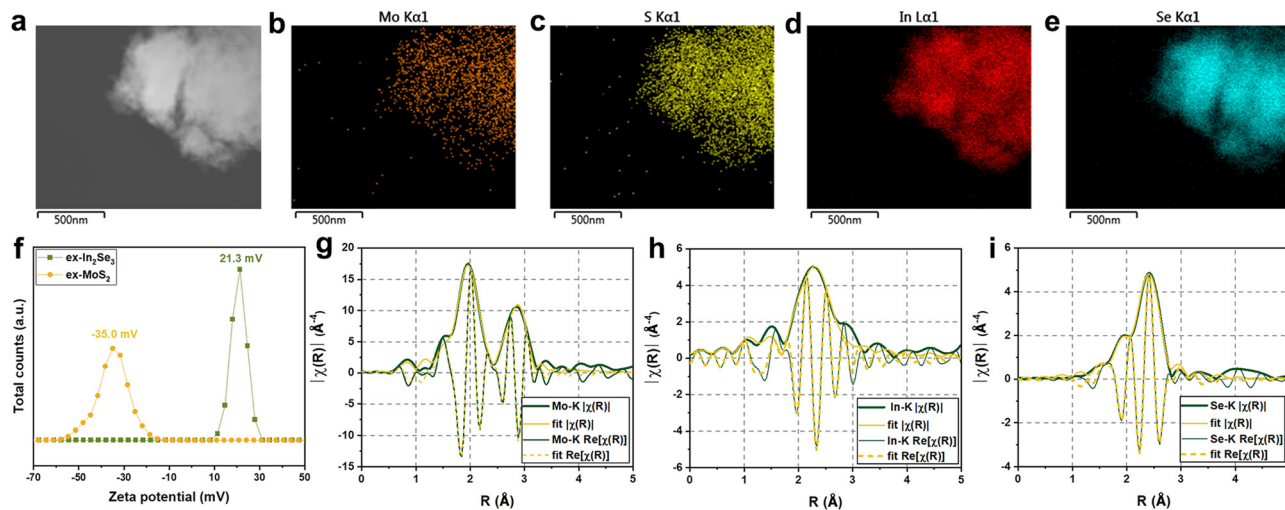
Fig. 2 (a) TEM image of MoS_2–In_2Se_3 multi-heterojunction and its EDX mapping of Mo (b) and S (c), In (d), Se (e). (f) Zeta potential of ex-In_2Se_3 and ex-MoS_2. (g–i) Fourier transform of k^3-weighted Mo (g), In (h), Se (i) K-edge of EXAFS spectra of MoS_2–In_2Se_3 multi-heterojunction.

the positively charged surface of an ex-In_2Se_3 flake clearly harmonises with the expected substantial anion defective monolayer, as discussed. Such a large difference in the chemical propensity of different chalcogens towards Li can enable self-assembly of ex-In_2Se_3 and ex-MoS_2 monolayers to prepare multi-heterojunction *via* layer-by-layer re-stacking using their opposite zeta potential in a solution of controlled pH.

As a result of mixing two solutions containing individual MoS_2 and In_2Se_3 monolayers for a period of time a solid precipitate was collected. TEM images (Fig. 2a) show thicker patches compared to the single layer fakes (Fig. S1, ESI†). Its EDX mapping (Fig. 2b–e) has shown a homogeneous mixture between the Mo, S, In and Se, indicative of restacking of the individual layers. Mo, In and Se K-edge extended X-ray absorption fine structure (EXAFS) analyses of the MoS_2–In_2Se_3 multi-heterojunction sample were carried out. All the fitting parameters along with their *k*-space data and fits have been provided in ESI† Fig. S10 and Table S3a–c. First, Mo–S and Mo–Mo short and long scattering paths can be well-fitted for the Mo K-edge data (Fig. 2g). For Mo–S and Mo–Mo, the average coordination number for both paths is found to approach 6.0, which is similar to that for the MoS_2 structure.[46] However, additional interactions between Mo–Se and Mo–In can be clearly evident, with small but distinctive coordination numbers of 0.38 and 0.30, respectively. Moreover, the scattering path of In–Se is determined with an average coordination number of 2.85 according to In K-edge data (Fig. 2h), which is significantly lower than the theoretical monolayer figure for In_2Se_3 of 4.0 but is consistent with the Se leached monolayer. Interestingly as shown in Fig. 2i, an additional

scattering path of In–S is deduced with a coordination number of 1.15. This clearly depicts the scrambling of atoms between these monolayers in their mixture. It appears that MoS_2 has mostly retained its structure in the multi-heterojunction sample, while In_2Se_3 shows noteworthy integration into the MoS_2 species due to its substantial defective nature as discussed above. Although the bond length for Mo–Se obtained from data fitting of the Mo and Se K-edge (Fig. 2i) differs only by 0.01 Å, their evaluated coordination number diverges. One possible final assembly structure according to EXAFS data is an alternating restacking of the apparently intact MoS_2 monolayer with decorated Se-defect In_2Se_3 layer-by-layer by electrostatic interaction: the missing Se sites of defective In_2Se_3 with exposed In atoms have been substituted by S atoms from MoS_2 at the interface. The rigidity of individual layers is not yet known, hence it would be interesting to determine the spatial arrangement in future. Nevertheless, this results in the clear emergence of Mo–S/Se–In motifs at the interface of the MoS_2–In_2Se_3 multi-heterojunction.

Density functional theory (DFT) calculations

Layer-by-layer periodic DFT calculations of these two heterogeneous metal chalcogenide monolayers in a 2H arrangement (trigonal prismatic) were carried out to guide our understanding of the restacked structure using the Perdew–Burke–Ernzerhof (PBE),[47] exchange correlation functional and a D3 dispersion correction[48] by means of the Vienna *Ab initio* Simulation Package (VASP).[49] Most structures were obtained from the Materials Project open dataset,[50] and the crystal structure manipulations were done by using the Python Materials Genomics package
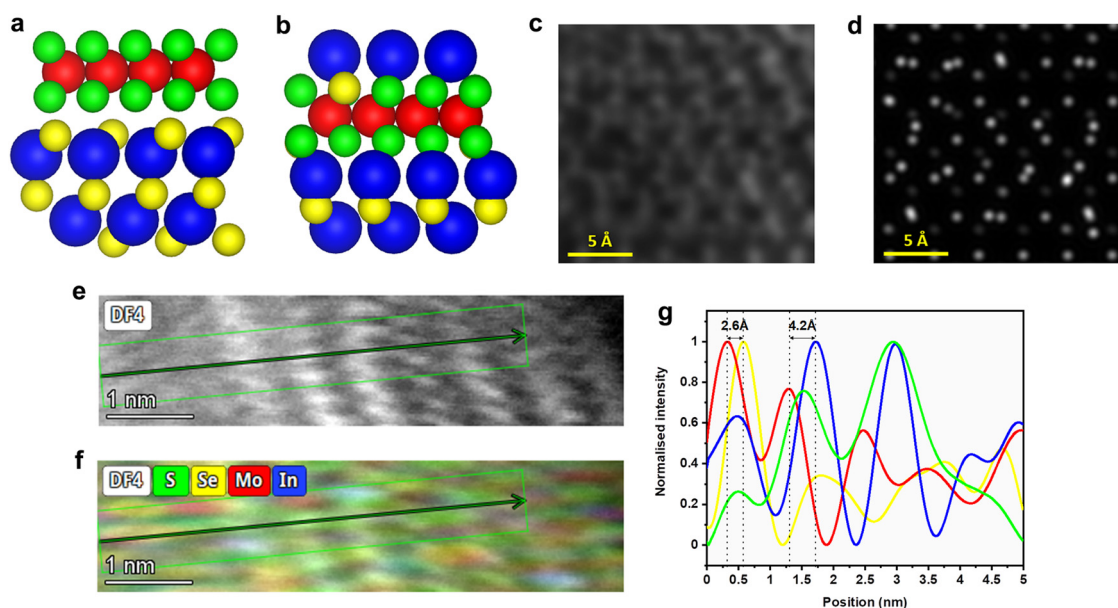
Fig. 3 (a) Bulk model for MoS_2–In_2Se_3 monolayer stacking. (b) Stacking of alternative MoS_2 layer with a 12.5% Se substitution into S of "In–Se" layer. Colour scheme: Red = Mo, Green = S, Blue = In, Yellow = Se. (c) Experimental HAADF-STEM image of MoS_2–In_2Se_3. (d) Simulated HAADF-STEM image with (c). (e) Super EDX of MoS_2–In_2Se_3 near surface assembly. The upper left side of figures are HAADF and (f) elements mapping by EDX superimposed on the experimental images as insets. Colour scheme: Red = Mo, Green = S, Blue = In, Yellow = Se. Although the layer assembly was not flat with reference to the beam direction (distorting peak sizes), one can see the Mo–S and In–Se in 2H arrangements resembling to their atomic distances (g). It is also interesting to reveal that the intimate Mo–Se (2.6 Å) and Mo–In (4.2 Å) atomic distances resembles to that in the optimised DFT model with 12.5% S substitution with Se within experimental error.

940 | *Mater. Chem. Front.*, 2023, **7**, 937–945

This journal is © The Royal Society of Chemistry and the Chinese Chemical Society 2023

(pymatgen)[51] and Atomic Simulation Environment (ASE).[52] For bulk geometry relaxation, a plane-wave basis set was used with a kinetic energy cut-off of 520 eV, and electronic and force convergence tolerances of 10^{-6} eV and 10^{-3} eV·Å^{-1}, respectively, were imposed. Further computational details and a description of the computational models are provided in the ESI.† Calculations were applied to validate the model and to ensure its stability.

Restacking of alternating monolayers of intact In$_2$Se$_3$ and MoS$_2$ is first subjected to geometry optimisation (Fig. 3a). The bond lengths and coordination numbers obtained in this optimised model were clearly found to deviate from the derived bond lengths and coordination numbers from EXAFS fitting. Given the substantial Se defective structures determined by EDX, a model was built by removing the top or/and bottom Se layers of In$_2$Se$_3$, and alternating this "In$_2$Se" with MoS$_2$ layers with different degrees of Se substitution into S at the interface (Fig. 3b). This model incorporates the Mo–S/Se–In motifs in line with the EXAFS fitting into the structure. Using the 2H MoS$_2$, three sub-models with 6.3%, 12.5% and 25.0% of S substituted by Se atoms were generated, and subject to geometry relaxation, with the bond distances between pairs of atoms summarized in Table 1. The results are promising, with most bond distances best matched to the EXAFS data for the 12.5% case, evidenced by the highest R-factor. Such a DFT optimised structure was then used to simulate an expected HAADF image (Fig. 3c), which also shows a good agreement with the experimental image in Fig. 3d. To further confirm the inter-atomic mixing between the two phases, high-resolution super-EDX mapping using a ThermoFisher Themis Z300 scanning transmission electron microscope equipped with highly sensitive Super-X energy dispersive X-ray spectrometer containing a high-speed, high-throughput, quad-silicon drift detector optimized for rapid X-ray collection (0.9 srad) and when combined with STEM to enable EDS spectral mapping down to the atomic scale. This facility was particularly employed to obtain the spatial elemental mapping of the near surface multi-heterojunction. The images reveal distinct dispersion of S, Se, Mo, In atoms on a selected flake surface according to their characteristic EDX emissions (Fig. 3e, f and ESI† Fig. S11). Such spatial differentiation of Super-EDX, allows us to delve into an

atomic level (Fig. 3g). The corresponding spatial atomic distances between Mo–Se and Mo–In (2.6 Å and 4.2 Å) match with the optimised DFT model (2.6 Å and 4.0 Å) within experimental errors.

As stated, experimentally from EDX, we found that In$_2$Se$_3$ has a higher tendency to form anion defects compared to MoS$_2$. The vacancy formation energies for In$_2$Se$_3$ and MoS$_2$ have also been calculated to understand the energy cost associated with anion defect formation, with their bulk phase used as the reference point to justify our experimental results. It was calculated as $E_f = E_{\text{sys-vac}} - E_{\text{sys}} + \mu_i$, where $E_{\text{sys-vac}}$ and E_{sys} are the total energies of the vacancy-containing and the stoichiometric configurations, respectively, and μ_i is the chemical potential of the atom i removed to generate the vacancy. This calculation was done on all atoms in bulk MoS$_2$, In$_2$Se$_3$, and stacked MoS$_2$–In$_2$Se$_3$ multi-heterojunctions, with the results summarized in Table S4 (ESI†). Coincidentally, the calculated anion vacancy formation energies for MoS$_2$ and In$_2$Se$_3$ are 2.86 eV and 0.53 eV, respectively, comparatively much lower than those for cations at energies higher than 3 eV. This aligns with the fact that Mo and S have higher bonding strengths compared to In and Se and the selective oxidative leaching of bulky Se atoms rather than S can also be justified theoretically. Thus, defect formation during the Li treatment will therefore be more energy costly in MoS$_2$ compared to In$_2$Se$_3$. Likewise, this fact agrees with our observation of a highly Se defective exfoliated ex-In$_2$Se$_3$.
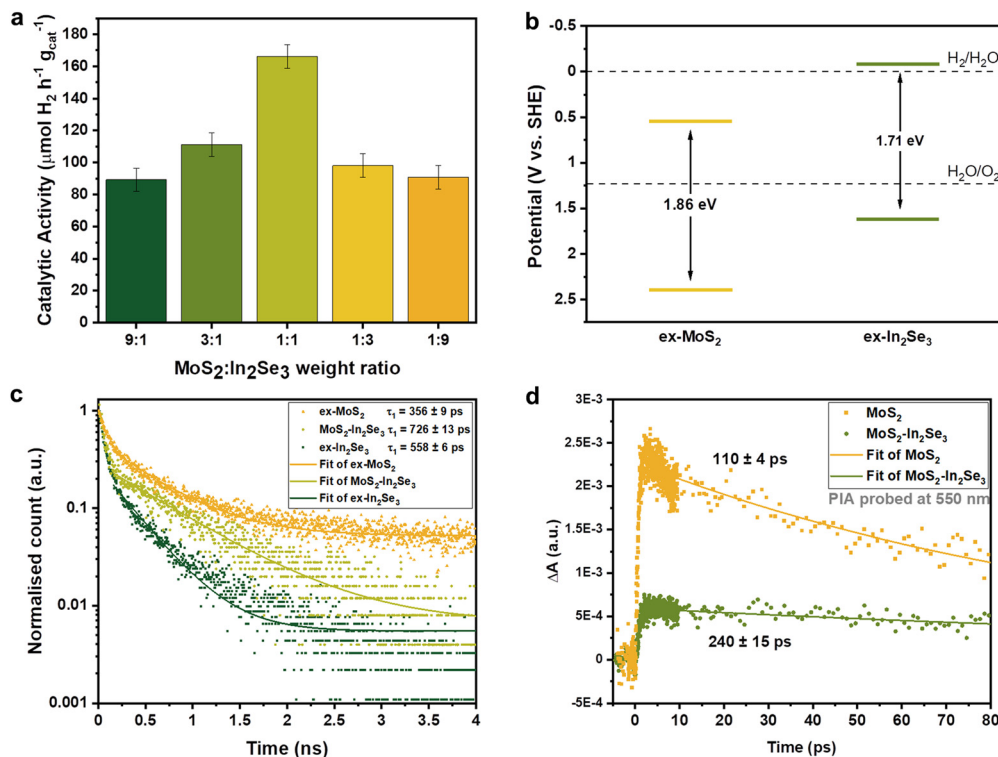
Photocatalysis of water splitting

MoS$_2$ is known to catalyze photo-water splitting to H$_2$/O$_2$ due to its facile polarization.[41,53] In order to demonstrate the potential use of modified MoS$_2$ layers upon formation of multi-heterojunction with other metal chalcogenide layers, photo-catalytic water splitting was studied with different weight ratios of ex-In$_2$Se$_3$ and ex-MoS$_2$ (Fig. 4a). The photo-catalytic water splitting has its maximum seen at a 1:1 weight ratio between a mixture of ex-MoS$_2$ and ex-In$_2$Se$_3$, compared to the different weight ratio. Evidently, the re-stacking of alternating layers of MoS$_2$ and In$_2$Se$_3$ with different potential energy levels should, in principle, have a strong promoting effect on photo water splitting due to the enhanced exciton separation by the 1:1 multi-heterojunction. To confirm such optical interactions, a combination of ultraviolet photoelectron spectroscopy (UPS) and a Tauc plot were uesd to understand the position of the valence band and the conduction band of the materials. From the UPS spectra of ex-In$_2$Se$_3$ (ESI† Fig. S12a and b), its Fermi energy and cut-off energy are evaluated to be 5.81 and 20.97 eV, respectively. While for ex-MoS$_2$ (ESI† Fig. S12c and d), they are evaluated to be 5.20 and 19.90 eV, respectively. The energies of the valence band of ex-MoS$_2$ and ex-In$_2$Se$_3$ can be evaluated to be 2.40 eV and 1.62 eV above standard hydrogen electrode (SHE), respectively. From the Tauc plot (ESI† Fig. S13), the band gaps of the ex-MoS$_2$ and ex-In$_2$Se$_3$ sample are assessed to be 1.86 eV and 1.71 eV, respectively.[54,55] Then, a band-edge

Table 1 Comparison of bond length obtained from EXAFS fitting and optimised DFT model. All atomic distances are in Å

Bond	EXAFS/Å	Monolayer stacking^a	6.3%^{b}	12.5%^{b}	25.0%^{b}
Mo–In	3.97 (Mo K-edge)	5.94	4.16	4.07	4.23
Mo–Se	2.60 (Mo K-edge)	4.70	2.52	2.52	2.52
	2.61 (Se K-edge)				
Mo–S	2.40 (Mo K-edge)	2.40	2.37	2.37	2.37
Mo–Mo	3.17 (Mo K-edge)	3.16	3.11	3.10	3.11
In–Se	2.64 (In K-edge)	2.55	2.69	2.63	2.61
	2.60 (Se K-edge)				
In–S	3.01 (In K-edge)	4.34	2.85	2.88	2.74
	R-factor	0.748	0.987	0.994	0.980

^{a} MoS$_2$–In$_2$Se$_3$ monolayer stacking (Fig. 3a). ^{b} Alternating MoS$_2$ and "In$_2$Se" layer with different degree of Se substitution of S.

Fig. 4 (a) Rate of photocatalytic water splitting at 270 °C for 9 : 1, 3 : 1, 1 : 1, 1 : 3, and 1 : 9 weight ratio between ex-MoS_2 and ex-In_2Se_3. (b) Band diagram of MoS_2–In_2Se_3 multi-heterojunction. (c) TRPL of ex-MoS_2, MoS_2–In_2Se_3 and ex-In_2Se_3. The solid lines are fit of data with single-exponential decay. (d) PIA of MoS_2–In_2Se_3 and ex-MoS_2 probed at 550 nm under 400 nm excitation. The solid lines are fit of data with single-exponential decay.

diagram for the MoS_2–In_2Se_3 multi-heterojunction was constructed (Fig. 4b).

Time-resolved photoluminescence (TRPL) was performed to determine the lifetime of the excitons (Fig. 4c). The typical TRPL profile could be fitted with single or multifunctional exponential decay curve. As far as the high background noise as concern, there could introduce a significantly higher degree of errors if a multifunctional decay curve is fitted. As a result, for simplicity, we have used a single exponential fit for the comparison. It is found that the lifetime obtained from fitting a single-exponential decay to the MoS_2–In_2Se_3 multi-heterojunction emission (726 ps) is indeed significantly longer than that for ex-MoS_2 (356 ps) and ex-In_2Se_3 (558 ps). Transient absorption spectroscopy (TAS) is used to investigate the behaviour of the photoexcited charges in the heterojunction. 2D TAS spectra (ESI† Fig. S14) show that the photoexcitation dynamic process of the conduction band electrons of the MoS_2–In_2Se_3 heterojunction is similar to that of ex-MoS_2 with generally lower intensities. This reiterates the similarity between the structure of the more retained MoS_2 in the MoS_2–In_2Se_3 multi-heterojunction. Photo-induced absorption (PIA, i.e., $\Delta A > 0$) decay is monitored to examine the dynamic population of the excited states in the conduction band for both a MoS_2–In_2Se_3 heterojunction and ex-MoS_2. PIA signals probed at 550 nm and 705 nm (Fig. 4d and ESI† Fig. S15) both show that the recombination lifetimes of the carriers in MoS_2–In_2Se_3 are longer than that of ex-MoS_2 (240 ps for MoS_2–In_2Se_3 and 110 ps for MoS_2), consistent with the results from TRPL. The defective In_2Se layers can therefore exert a promoting effect on

the lifetime of the excitons when decorated on MoS_2 layers, which in turn explains the higher catalytic activity for water splitting when compared to the ex-In_2Se_3 and ex-MoS_2.

Conclusion

In conclusion, we have identified a new chemical method which can prepare layer-by-layer assembly from monolayer sheets in solution. The specific electrostatic attraction between different chalcogenide layers and different leaching and polarization extents can be used to prepare an AB-type of restacking without much phase segregation. To demonstrate the potential use of such assembled materials, a photocatalyst with atomic layer-by-layer stacking with chemically exfoliated MoS_2 and In_2Se_3 is for the first time made, which is demonstrated to give enhanced photocatalytic activity for photo water splitting due to prolonged exciton lifetime. It is anticipated that the described atomic layer-by-layer re-stacking in the chemical solution method may also be useful to synthesise mixed chalcogenide layers of other optoelectronic interests.

Methods

Exfoliation of MoS2

ex-MoS_2 single layers in solution was prepared based on our previous reports,[20,36,37] which is routed from a lithium intercalation-sonication method. Bulk-MoS_2 (2.00 g) was

942 | Mater. Chem. Front., 2023, 7, 937–945

This journal is © The Royal Society of Chemistry and the Chinese Chemical Society 2023

vigorously stirred in 16 mL of 1.6 M n-butyllithium/hexane under a nitrogen atmosphere for 48 hours. After washing with hexane to remove the unreacted n-butyllithium, the lithiated MoS_2 (Li_xMoS_2) was separated by centrifugation and followed by drying in $vacuo$ at 70 °C. The solid was then immersed into 250 mL of water and sonicated for 6 hours. The suspension was then centrifuged at 5000 rpm for 15 minutes to remove the unexfoliated precursors and only the supernatant was collected. HCl (37%) was then added dropwise to the collected supernatant until precipitates are formed at a pH of around 7. The solid was separated by centrifugation at 5000 rpm for 15 minutes and the exfoliated 2D-MoS_2 was obtained after drying in $vacuo$ overnight at 70 °C.

Exfoliation of In_2Se_3

The method of synthesizing ex-In_2Se_3 is developed adapted from the same method on the synthesis of monolayer MoS_2. Exfoliated 2D-In_2Se_3 is prepared with the standard lithium intercalation-sonication method. Bulk-In_2Se_3 (2.00 g) was vigorously stirred in 16 mL of 1.6 M n-butyllithium/hexane under a nitrogen atmosphere for 72 hours. After washing with hexane to remove the unreacted n-butyllithium, the lithiated In_2Se_3 ($Li_xIn_2Se_3$) was separated by centrifugation and followed by drying in $vacuo$ at 70 °C. The solid was then immersed into 250 mL of water and sonicated for 6 hours (with a power output of 35 W and an operating frequency at 37 kHz, Elma Schmidbauer, Germany). The suspension was then centrifuged at 5000 rpm for 15 minutes to remove the unexfoliated precursors and only the supernatant was collected. HCl (37%) was then added dropwise to the collected supernatant until precipitates were formed at a pH of around 7. The solid was separated by centrifugation at 5000 rpm for 15 minutes and the exfoliated 2D-In_2Se_3 was obtained after drying in $vacuo$ overnight at 70 °C.

Synthesis of MoS_2–In_2Se_3

The multi-heterojunction was fabricated through a facile electrostatic self-assembly approach.[56] Five MoS_2–In_2Se_3 samples were prepared with different weight ratios: 9 : 1, 3 : 1, 1 : 1, 1 : 3 and 1 : 9 for prolonged precipitation. The as-prepared 2D-MoS_2 sample (250 mg) was first added to aqueous HCl solution (100 mL, 1.5 M) and sonicated for 1 hour, followed by vigorous stirring for 4 hours for further protonation. The resulting acidified suspension was separated by centrifugation at 5000 rpm for 15 minutes and was washed with deionised water until neutral to remove superfluous HCl. The acidified sample was re-dispersed into 100 mL of deionised water. According to the weight ratio, a certain amount of ex-In_2Se_3 portion was added. The mixture was sonicated for 30 minutes and then stirred vigorously for another 4 hours. The resulting product was allowed to precipitate and centrifuged at 5000 rpm for 15 minutes and was dried in $vacuo$ overnight at 70 °C.

Author contributions

C. C. Y. W. and W. N. performed synthesis and catalyst testing; B. K. Y. N. and K. T. carried out EXAFS analysis; H. P. G. and

M. S. for DFT calculations; P.-L. H. and W. C. H. K. performed HAADF-STEM analysis; Y. L. and R. A. T. for TRPL analysis; M. L. for TAS and PIA analysis; B. K. Y. N. and S. C. E. T. wrote the main text. All authors have given approval to the final version of the manuscript. S. C. E. T. planned, supervised and led the project.

Conflicts of interest

There are no conflicts to declare.

Acknowledgements

References

1 R. Roldán, et $al.$, Electronic properties of single-layer and multilayer transition metal dichalcogenides MX2 (M = Mo, W and X = S, Se), $Ann.$ $Phys.$, 2014, **526**, 347–357, DOI: **10.1002/andp.201400128**.

2 M. Chhowalla, et $al.$, The chemistry of two-dimensional layered transition metal dichalcogenide nanosheets, $Nat.$ $Chem.$, 2013, **5**, 263–275, DOI: **10.1038/nchem.1589**.

3 J. V. Vaghasiya, K. Kripalova, S. Hermanova, C. C. Mayorga-Martinez and M. Pumera, Real-Time Biomonitoring Device Based on 2D Black Phosphorus and Polyaniline Nanocomposite Flexible Supercapacitors, $Small$, 2021, **17**, e2102337, DOI: **10.1002/smll.202102337**.

4 J. V. Vaghasiya, C. C. Mayorga-Martinez, J. Vyskočil, Z. Sofer and M. Pumera, Integrated Biomonitoring Sensing with Wearable Asymmetric Supercapacitors Based on Ti3C2 MXene and 1T-Phase WS2 Nanosheets, $Adv.$ $Funct.$ $Mater.$, 2020, **30**, 2003673, DOI: **10.1002/adfm.202003673**.

5 K. Ghosh and M. Pumera, MXene and MoS(3-) (x) Coated 3D-Printed Hybrid Electrode for Solid-State Asymmetric Supercapacitor, $Small$ $Methods$, 2021, **5**, e2100451, DOI: **10.1002/smtd.202100451**.

6 J. Vyskočil, et $al.$, 2D Stacks of MXene Ti3C2 and 1T-Phase WS2 with Enhanced Capacitive Behavior, $ChemElectroChem$, 2019, **6**, 3982–3986, DOI: **10.1002/celc.201900643**.

7 N. Rohaizad, C. C. Mayorga-Martinez, M. Fojtu, N. M. Latiff and M. Pumera, Two-dimensional materials in biomedical, biosensing and sensing applications, $Chem.$ $Soc.$ $Rev.$, 2021, **50**, 619–657, DOI: **10.1039/d0cs00150c**.

8 A. Kutana, E. S. Penev and B. I. Yakobson, Engineering electronic properties of layered transition-metal dichalcogenide compounds through alloying, $Nanoscale$, 2014, **6**, 5820–5825, DOI: **10.1039/c4nr00177j**.

9 J. Lauritsen, *et al.*, Location and coordination of promoter atoms in Co- and Ni-promoted MoS2-based hydrotreating catalysts, *J. Catal.*, 2007, **249**, 220–233, DOI: **10.1016/j.jcat.2007.04.013**.

10 C. Cui, *et al.*, Intercorrelated In-Plane and Out-of-Plane Ferroelectricity in Ultrathin Two-Dimensional Layered Semiconductor In2Se3, *Nano Lett.*, 2018, **18**, 1253–1258, DOI: **10.1021/acs.nanolett.7b04852**.

11 D. Andrzejewski, *et al.*, Scalable Large-Area p–i–n Light-Emitting Diodes Based on WS2 Monolayers Grown via MOCVD, *ACS Photonics*, 2019, **6**, 1832–1839, DOI: **10.1021/acsphotonics.9b00311**.

12 B. Liu, *et al.*, Chemical Vapor Deposition Growth of Mono-layer WSe2 with Tunable Device Characteristics and Growth Mechanism Study, *ACS Nano*, 2015, **9**, 6119–6127.

13 S. Cwik, *et al.*, Direct Growth of MoS2 and WS2 Layers by Metal Organic Chemical Vapor Deposition, *Adv. Mater. Interfaces*, 2018, **5**, 1800140, DOI: **10.1002/admi.201800140**.

14 J. H. Han, S. Lee and J. Cheon, Synthesis and structural transformations of colloidal 2D layered metal chalcogenide nanocrystals, *Chem. Soc. Rev.*, 2013, **42**, 2581–2591, DOI: **10.1039/c2cs35386e**.

15 S. M. Tan, C. C. Mayorga-Martinez, Z. Sofer and M. Pumera, Bipolar Electrochemistry Exfoliation of Layered Metal Chal-cogenides Sb2 S3 and Bi2 S3 and their Hydrogen Evolution Applications, *Chemistry*, 2020, **26**, 6479–6483, DOI: **10.1002/chem.201904767**.

16 J. Zheng, *et al.*, High yield exfoliation of two-dimensional chalcogenides using sodium naphthalenide, *Nat. Commun.*, 2014, **5**, 2995, DOI: **10.1038/ncomms3995**.

17 J. N. Coleman, *et al.*, Two-dimensional nanosheets pro-duced by liquid exfoliation of layered materials, *Science*, 2011, **331**, 568–571, DOI: **10.1126/science.1194975**.

18 J. Zheng, *et al.*, Fe on molecular-layer MoS2 as inorganic Fe-S2-Mo motifs for light-driven nitrogen fixation to ammonia at elevated temperatures, *Chem. Catal.*, 2021, **1**, 162–182, DOI: **10.1016/j.checat.2021.03.002**.

19 J. Mo, *et al.*, Transition metal atom–doped monolayer MoS2 in a proton-exchange membrane electrolyzer, *Mater. Today Adv.*, 2020, **6**, 100020, DOI: **10.1016/j.mtadv.2019.100020**.

20 T. H. M. Lau, *et al.*, Engineering Monolayer 1T-MoS2 into a Bifunctional Electrocatalyst via Sonochemical Doping of Isolated Transition Metal Atoms, *ACS Catal.*, 2019, **9**, 7527–7534, DOI: **10.1021/acscatal.9b01503**.

21 R. Wang, *et al.*, Synthesis of In2Se3 homojunction photo-catalyst with α and γ phases for efficient photocatalytic performance, *Mater. Des.*, 2018, **151**, 74–82, DOI: **10.1016/j.matdes.2018.04.052**.

22 K. S. Novoselov, *et al.*, Electric Field Effect in Atomically Thin Carbon Films, *Science*, 2004, **306**, 666–669.

23 V. Nicolosi, M. Chhowalla, M. G. Kanatzidis, M. S. Strano and J. N. Coleman, Liquid Exfoliation of Layered Materials, *Science*, 2013, **340**, 6139, DOI: **10.1126/science.1194975**.

24 G. Eda, *et al.*, Photoluminescence from chemically exfo-liated MoS2, *Nano Lett.*, 2011, **11**, 5111–5116, DOI: **10.1021/nl201874w**.

25 G. Du, *et al.*, Superior stability and high capacity of restacked molybdenum disulfide as anode material for lithium ion batteries, *Chem. Commun.*, 2010, **46**, 1106–1108, DOI: **10.1039/b920277c**.

26 R. Bissessur and H. Xu, Nanomaterials based on molybde-num diselenide, *Mater. Chem. Phys.*, 2009, **117**, 335–337, DOI: **10.1016/j.matchemphys.2009.06.030**.

27 D. Sudha and P. Sivakumar, Review on the photocatalytic activity of various composite catalysts, *Chem. Eng. Process.*, 2015, **97**, 112–133, DOI: **10.1016/j.cep.2015.08.006**.

28 J. Low, J. Yu, M. Jaroniec, S. Wageh and A. A. Al-Ghamdi, Heterojunction Photocatalysts, *Adv. Mater.*, 2017, **29**, 1601694, DOI: **10.1002/adma.201601694**.

29 C. Gao, *et al.*, A Photoresponsive Rutile TiO2 Heterojunction with Enhanced Electron-Hole Separation for High-Performance Hydrogen Evolution, *Adv. Mater.*, 2019, **31**, e1806596, DOI: **10.1002/adma.201806596**.

30 M.-L. Tsai, *et al.*, Monolayer MoS2 Heterojunction Solar Cells, *ACS Nano*, 2014, **8**, 8317–8322.

31 X. Zhang, *et al.*, Vertical heterostructures of layered metal chalcogenides by van der Waals epitaxy, *Nano Lett.*, 2014, **14**, 3047–3054, DOI: **10.1021/nl501000k**.

32 R. Cheng, *et al.*, Electroluminescence and photocurrent generation from atomically sharp WSe2/MoS2 heterojunc-tion p-n diodes, *Nano Lett.*, 2014, **14**, 5590–5597, DOI: **10.1021/nl502075n**.

33 X. Zhao, *et al.*, Engineering covalently bonded 2D layered materials by self-intercalation, *Nature*, 2020, **581**, 171–177, DOI: **10.1038/s41586-020-2241-9**.

34 P. Woanseo, *et al.*, Photoelectron Spectroscopic Imaging and Device Applications of Large-Area Patternable Single-Layer MoS2 Synthesized by Chemical Vapor Deposition, *ACS Nano*, 2014, **8**, 4961–4962.

35 J. Wu, *et al.*, Large thermoelectricity via variable range hopping in chemical vapor deposition grown single-layer MoS2, *Nano Lett.*, 2014, **14**, 2730–2734, DOI: **10.1021/nl500666m**.

36 G. Liu, *et al.*, MoS2 monolayer catalyst doped with isolated Co atoms for the hydrodeoxygenation reaction, *Nat. Chem.*, 2017, **9**, 810–816, DOI: **10.1038/nchem.2740**.

37 T. H. M. Lau, *et al.*, Transition metal atom doping of the basal plane of MoS2 monolayer nanosheets for electroche-mical hydrogen evolution, *Chem. Sci.*, 2018, **9**, 4769–4776, DOI: **10.1039/c8sc01114a**.

38 P. K. Mohapatra, K. Ranganathan, L. Dezanashvili, L. Houben and A. Ismach, Epitaxial growth of In2Se3 on monolayer transition metal dichalcogenide single crystals for high performance photodetectors, *Appl. Mater. Today*, 2020, **20**, 100734, DOI: **10.1016/j.apmt.2020.100734**.

39 R. Niranjan and N. Padha, Growth of γ- In2Se3 monolayer from multifaceted InxSey thin films via annealing and study of its physical properties, *Mater. Chem. Phys.*, 2021, **257**, 123823, DOI: **10.1016/j.matchemphys.2020.123823**.

40 J. Dr Barthel, Probe: A software for high-resolution STEM image simulation, *Ultramicroscopy*, 2018, **193**, 1–11, DOI: **10.1016/j.ultramic.2018.06.003**.

41 T. Jia, *et al.*, The remarkable activity and stability of a dye-sensitized single molecular layer MoS2 ensemble for photo-catalytic hydrogen production, *Chem. Commun.*, 2015, **51**, 13496–13499, DOI: **10.1039/c5cc03871e**.

42 S. D. Setzler, *et al.*, Observation of singly ionized selenium vacancies in ZnSe grown by molecular beam epitaxy, *Appl. Phys. Lett.*, 1997, **70**, 2274–2276, DOI: **10.1063/1.118836**.

43 T. A. Kennedy, *et al.*, Identification ofVSe-impurity pairs in ZnSe:N, *Appl. Phys. Lett.*, 1994, **65**, 1112–1114, DOI: **10.1063/1.112114**.

44 K. M. Beck, W. R. Wiley, E. Venkatasubramanian and F. Ohuchi, Vacancies ordered in screw form (VOSF) and layered indium selenide thin film deposition by laser back ablation, *Appl. Surf. Sci.*, 2009, **255**, 9707–9711, DOI: **10.1016/j.apsusc.2009.04.054**.

45 W. Shi, *et al.*, Near-infrared photoluminescent flowerlike α-In2Se3 nanostructures from a solvothermal treatment, *Chem. Eng. J.*, 2013, **225**, 474–480, DOI: **10.1016/j.cej.2013.03.066**.

46 B. Lassalle-Kaiser, *et al.*, Evidence from in situ X-ray absorption spectroscopy for the involvement of terminal disulfide in the reduction of protons by an amorphous molybdenum sulfide electrocatalyst, *J. Am. Chem. Soc.*, 2015, **137**, 314–321, DOI: **10.1021/ja510328m**.

47 J. P. Perdew, K. Burke and M. Ernzerhof, Generalized Gradient Approximation Made Simple, *Phys. Rev. Lett.*, 1996, **77**, 3865–3868.

48 S. Grimme, J. Antony, S. Ehrlich and H. Krieg, A consistent and accurate ab initio parametrization of density functional dispersion correction (DFT-D) for the 94 elements H-Pu, *J. Chem. Phys.*, 2010, **132**, 154104, DOI: **10.1063/1.3382344**.

49 G. Kresse and J. F. Furthmuller, Efficient iterative schemes for ab initio total-energy calculations using a plane-wave basis set, *Phys. Rev. B: Condens. Matter Mater. Phys.*, 1996, **54**, 11169–11186.

50 J. Paier, R. Hirschl, M. Marsman and G. Kresse, The Perdew-Burke-Ernzerhof exchange-correlation functional applied to the G2-1 test set using a plane-wave basis set, *J. Chem. Phys.*, 2005, **122**, 234102, DOI: **10.1063/1.1926272**.

51 S. P. Ong, *et al.*, Python Materials Genomics (pymatgen): A robust, open-source python library for materials analysis, *Comput. Mater. Sci.*, 2013, **68**, 314–319, DOI: **10.1016/j.commatsci.2012.10.028**.

52 A. Hjorth Larsen, *et al.*, The atomic simulation environment-a Python library for working with atoms, *J. Phys.: Condens. Matter*, 2017, **29**, 273002, DOI: **10.1088/1361-648X/aa680e**.

53 B. Hinnemann, P. G. Moses, J. Bonde, K. P. Jorgensen, J. H. Nielsen, S. Horch, I. Chorkendorff and J. K. Norskov, Biomimetic Hydrogen Evolution: MoS2 Nanoparticles as Catalyst for Hydrogen Evolution, *J. Am. Chem. Soc.*, 2005, **127**, 5308–5309.

54 F. Lyu, *et al.*, Thickness-dependent band gap of alpha-In2Se3: from electron energy loss spectroscopy to density functional theory calculations, *Nanotechnology*, 2020, **31**, 315711, DOI: **10.1088/1361-6528/ab8998**.

55 E. F. Procopio, R. N. Pedrosa, F. A. L. de Souza, W. S. Paz and W. L. Scopel, Tuning the photocatalytic water-splitting capability of two-dimensional alpha-In2Se3 by strain-driven band gap engineering, *Phys. Chem. Chem. Phys.*, 2020, **22**, 3520–3526, DOI: **10.1039/c9cp06023e**.

56 D. Zhao, *et al.*, Boron-doped nitrogen-deficient carbon nitride-based Z-scheme heterostructures for photocatalytic overall water splitting, *Nat. Energy*, 2021, **6**, 388–397, DOI: **10.1038/s41560-021-00795-9**.